*High Power Laser Science and Engineering*, (2025), Vol. 13, e44, 6 pages.
doi:10.1017/hpl.2025.32

HIGH POWER LASER SCIENCE AND ENGINEERING

RESEARCH ARTICLE

# Eight-pass neodymium-doped yttrium aluminum garnet laser amplifier at the 5 J level

Xinxing Lei[1,2], Zhou Dai[3], Xiaokai Huang[4], Yumei Zhang[4], Suyang Wang[1,2], Yuhang Li[1,2], Qiang Liu[1,2], and Xing Fu[1,2]

[1]*Department of Precision Instrument, Tsinghua University, Beijing, China*

[2]*State Key Laboratory of Precision Space-time Information Sensing Technology, Beijing, China*

[3]*Weixian College, Tsinghua University, Beijing, China*

[4]*DFH Satellite Co., Ltd., Beijing, China*

*(Received 9 January 2025; revised 10 March 2025; accepted 2 April 2025)*

**Abstract**

This paper presents an innovative eight-pass laser amplifier design that effectively utilizes polarization and angular multiplexing, enjoying high gain, high extraction efficiency and compact layout. To optimize the design parameters, a general spatiotemporal model for a multi-pass amplifier is established that accounts for beam passages in different angles, and the predicted output energy and gain distribution agree well with the experimental results. The multi-pass amplifier scales the seed energy of 120 mJ to 5 J at 10 Hz and 3 J at 50 Hz, with the beam quality within three times the diffraction limit.

**Keywords:** joule level; laser amplifier; multi-pass; nanosecond

## 1. Introduction

High-repetition-rate nanosecond pulse lasers with energies above the joule level have extensive applications in industry, medicine and scientific research[1–3]. To amplify the pulse energy of a seed laser, typically in the range of tens of millijoules to several joules, an approximate gain of 50–100 is necessary. To obtain such a high gain, the traditional single-pass multi-stage amplification approach inevitably leads to a low extraction efficiency and high system complexity. Instead, employing the multi-pass amplifier provides an effective solution that can simultaneously achieve high gain and high extraction efficiency.

Methods of realizing multiple beam passages that extract the gain generally fall into two categories: (1) polarization multiplexing using polarizing beam splitters (PBSs) and different polarization states[4], with routine devices to alter polarization states, such as wave plates, Faraday rotators, electro-optic switches and birefringent crystals; (2) angular multiplexing through varying deflection angles, which can be subdivided into near-field[5] and far-field cases[6]. Certainly, two types of multiplexing can be combined to yield more beam passages. For example, the most common four-pass amplifier scheme adopts a quarter-wave plate or a Faraday rotator in conjunction with PBSs. In a further step, by converting the gain medium from a transmissive to a reflective configuration in the active mirror geometry[7], an eight-pass transmissive gain extraction can be realized. Using this approach, a pulsed laser output of 1 J was achieved at the repetition rate of 10 Hz[8]. In addition, a four-pass configuration combined with angular multiplexing was utilized to achieve eight-pass scaling, leading to an output energy of 305 mJ at 10 Hz[9]. Furthermore, electro-optic switches and birefringent crystals were combined in a four-pass configuration to realize two distinct eight-pass amplification designs, yielding output energies of 2.7 J[10] and 2.5 J[11], respectively, at a repetition rate of 1 Hz. However, due to the limitations imposed by the laser-induced damage threshold (LIDT), further enhancement in energy necessitates an expansion of the aperture size. While large-aperture Faraday rotators (e.g., gas-cooled ceramic terbium gallium garnet designs[12]) can overcome strict aperture constraints, their adoption in high-energy systems may be limited by practical challenges such as increased system complexity, thermal load management and cost. Amplifier designs that multiplexed various incidence angles have boosted the number of beam passages up to 16[13] and 20[14]; however, these necessitate a significant amount of space for separating the beamlets and setting up the optics.

Correspondence to: Q. Liu and X. Fu, Department of Precision Instrument, Tsinghua University, Beijing 100084, China. Emails: qiangliu@tsinghua.edu.cn (Q. Liu); fuxing@tsinghua.edu.cn (X. Fu)

In this work, a general spatiotemporal model for a multi-pass amplifier that accounts for angular multiplexing is established, guided by which, a compact eight-pass neodymium-doped yttrium aluminum garnet (Nd:YAG) amplifier is designed and built, employing polarization and angular multiplexing and being free of the constraints of small-aperture devices such as the Faraday rotator. The reported multi-pass amplifier design demonstrates an output energy of 5 J at 10 Hz and 3 J at 50 Hz, with the corrected beam quality within three times the diffraction limit, offering excellent beam expansion potential and power scaling capabilities.

## 2. Design and modeling

The schematic diagram of the eight-pass amplifier is illustrated in Figure 1(a), consisting of a PBS, a gain module, a pump array, a quarter-wave plate and two mirrors. The gain module includes two Nd:YAG slabs, an anti-reflection (AR) and a high-reflection (HR) fused silica window, forming the geometry of an active mirror, and utilizes immersion water cooling for efficient thermal management.

Figure 1(b) depicts the sequence of a laser beam passing through the gain medium, where 'f' and 'b' represent the forward and backward directions, respectively, and the color bar illustrates the number of beam passages within the gain medium, while the dashed line indicates the pump area. As depicted in Figure 1(c), the seed beam passes through the PBS and enters the module, undergoing double transmissions of the gain region in a V-shaped path. The outgoing beam is then reflected by a mirror, M1, and re-enters the module at a small off-axis angle, so that the third and fourth passages are spatially separated from the first two passages (represented in different colors in the figure). The output beam after four passages is then guided back along its original path by the polarization multiplexing that uses the mirror M2 and the quarter-wave plate, and experiences another four passages through the gain region before being reflected at the PBS.

The angle of incidence for the first passage is denoted as $\theta_1$ in Figure 1(c), while the remaining angles $\theta_2$ to $\theta_6$ can be determined using the law of reflection and refraction. According to geometric relationships, the displacements of the light rays at each surface that are denoted as $x_1$ to $x_3$ can be calculated. The total projection lengths on the front and rear surfaces of the gain slab are respectively expressed as follows:

$$\begin{cases} w_2 = \frac{D}{2\cos\theta_1} + \frac{D}{2\cos\theta_4} + x_2' + 2d_2\tan\theta_6, \\ w_3 = \frac{D}{2\cos\theta_1} + \frac{D}{2\cos\theta_4} + x_3, \end{cases} \tag{1}$$

where $D$ is the injecting beam width.

Note that the displacement within the gain medium enlarges as the slab thickness $d_2$ increases. Therefore, in order to maintain a sufficient overlap among eight passages, which is important for maximizing the extraction efficiency of stored energy, the slab thickness is constrained. In addition, the displacement is dependent on the beam deviation angle $\alpha$. A smaller $\alpha$ can reduce the displacement, but then it is necessary to enlarge the propagation distance $L_1$ in order to achieve beam separation in the angular multiplexing, implying a trade-off between the extraction efficiency and compactness.

In our design, we set $d_2 = 20$ mm, $L_1 = 400$ mm, $L_2 = 30$ mm, $\alpha = 7°$ and $\theta_1 = 40°$ so that the maximum displacement $x_2'$ within the gain medium reaches 10.4 mm, corresponding to 28% of the beam cross-section size, which is the projected length of the beam width ($D = 30$ mm), ensuring that two paths at different angles can be effectively separated while maintaining a compact configuration. The multiple beam passages within the gain medium form a trapezoid with the upper width of $w_2 = 65.0$ mm and the lower width of $w_3 = 49.4$ mm. To achieve optimal pump matching, the pump beam distribution is also designed as a divergent trapezoidal shape. The multi-pass extracting beams and the pumping region within the gain medium are illustrated in Figure 1(b).

Since the propagation time within the eight-pass amplifier (~0.2 ns) is shorter than the pulse width around 10 ns, the beams from different passages always experience temporal overlap. On the other hand, the use of angular multiplexing results in spatial displacements among the beam paths from different passages, leading to a complicated spatiotemporal overlap phenomenon.

Our previous work presented a spatiotemporal model of an active mirror amplifier[15], which describes the stored energy density and extracting beam intensity at different positions within the gain medium at various time slices. The model implements both temporal (with a temporal grid size of $\mathrm{d}t$) and spatial discretizations (with spatial grid sizes of $\mathrm{d}x$ and $\mathrm{d}z$ in two directions, respectively, where $\mathrm{d}l = \sqrt{\mathrm{d}x^2 + \mathrm{d}z^2}$), ensuring that the rays propagate along the grid diagonal, as represented by $\tan\theta = \mathrm{d}x/\mathrm{d}z$, where $\theta$ is the refraction angle in the gain medium. Furthermore, it must be satisfied that the exact time taken for the light to cross one spatial slice is $\mathrm{d}t = n\mathrm{d}l/c$, where $c$ is the speed of light in vacuum and $n$ is the refractive index of the gain medium. During the time interval of $T \to T + \mathrm{d}t$, the extracting beam intensity and the instantaneous stored energy density at different locations are expressed as follows[15]:

$$\begin{aligned} &I\left(nx_i\left(x,z,T\right), nt_i\left(x,z,T\right), T+\mathrm{d}t\right) \\ &\quad = G_\mathrm{e}\left(x,z,t\right) I\left(nx_i\left(x,z,T\right), nt_i\left(x,z,T\right), T\right), \end{aligned} \tag{2}$$

$$\begin{aligned} E_\mathrm{st}\left(x,z,T+\mathrm{d}t\right) &= E_\mathrm{st}\left(x,z,T\right) \\ &\quad - \left(G_\mathrm{e}\left(x,z,T\right) - 1\right) I_\mathrm{in}\left(x,z,t\right) \mathrm{d}t/\mathrm{d}l, \end{aligned} \tag{3}$$

where $E_\mathrm{st}\left(x,z,T\right)$ is the pump energy stored at the grid, $I_\mathrm{in}\left(x,z,t\right)$ is the cumulative intensity of all rays within

https://doi.org/10.1017/hpl.2025.32 Published online by Cambridge University Press

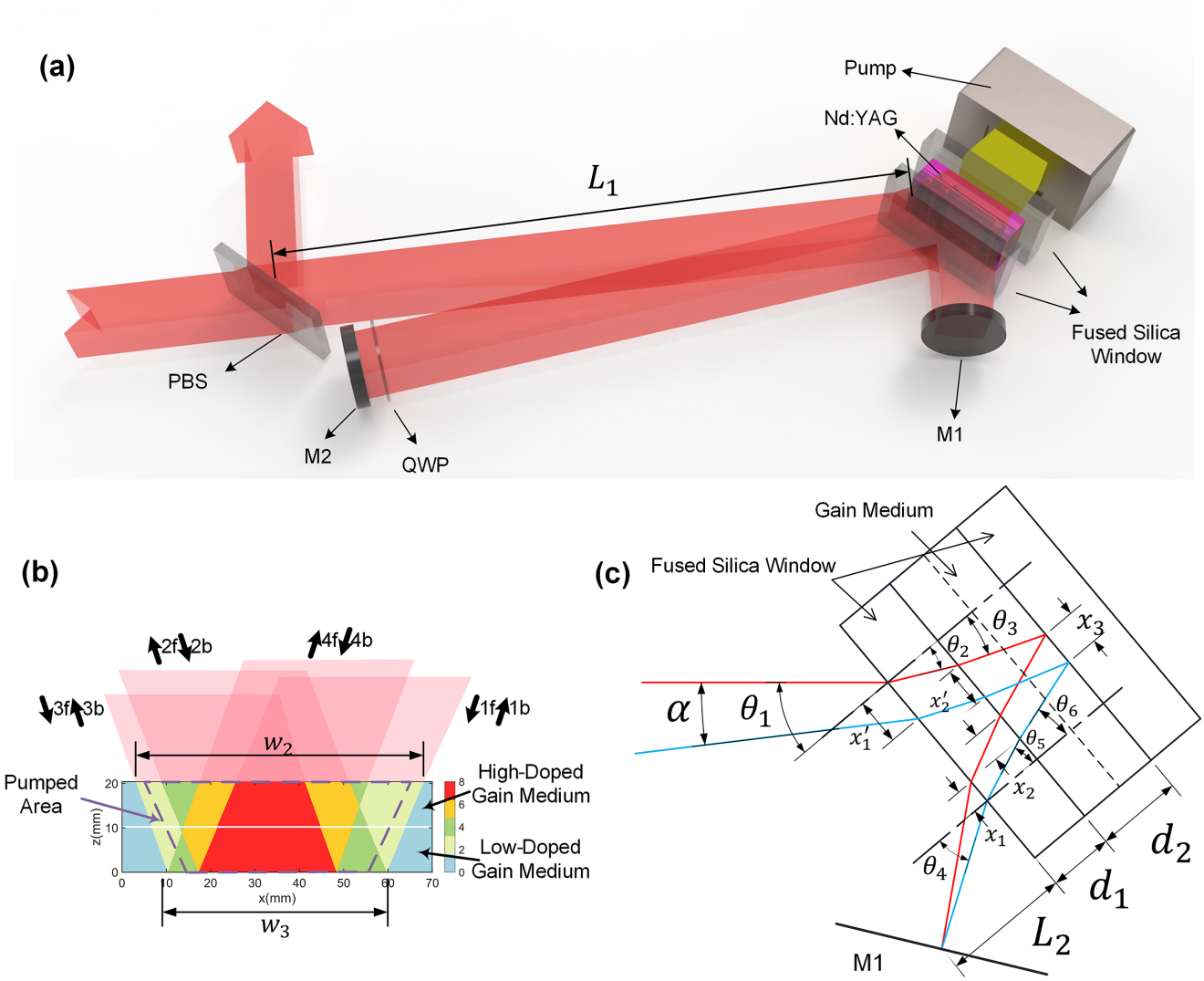


**Figure 1.** Schematic diagram of the eight-pass laser amplifier. (a) Optical layout. PBS, polarizing beam splitter; M1, M2, flat reflective mirrors; QWP, quarter-wave plate. (b) Sequence of the laser beam passing through the gain medium. (c) Propagation trajectory of the central ray in the gain module.

the grid and the gain $G_e(x, z, t)$ is calculated according to the Frantz–Nodvik equation, utilizing both $E_{st}(x, z, T)$ and $I_{in}(x, z, t)$.

However, the previous spatiotemporal model is not valid for the cases with angular multiplexing employed here. In this work, we extend the model to account for angular multiplexing in multi-pass power scaling. In contrast to adopting a single incidence angle and thus a single set of spatiotemporal grids for calculations in the previous model, the key to our new model is to simultaneously accommodate the successive propagation of rays at different angles. Specifically, we select one angle as the standard for grid division, where the ray propagation method is consistent with that of the previous model, referred to as the grid-matched ray, as illustrated in Figure 2(a). In this case, each step progresses by one grid unit along the $x$- and $z$-directions. Conversely, the ray at another angle is classified as non-grid-matched ray, as shown in Figure 2(b). In this case, ray tracing is required to determine the grids traversed by the light, with additional increments of d$x$ or d$z$ typically introduced at regular intervals. Simultaneously, the temporal grid size d$t$ exhibits a mismatch with the individual spatial grid, which necessitates a similar one-dimensional approach in the temporal dimension, whereby after each identical time interval, a step corresponds to two spatial grids. This approach enables the simultaneous transmission of two light beams with different angles within a set of grids, thereby allowing for the calculation of their overlapping amplification. Furthermore, this approach remains valid for more complex scenarios, such as a much higher degree of angular multiplexing.

## 3. Results and discussion

In the experiment, the seed beam has the maximum pulse energy of 120 mJ, the pulse width of 8 ns, an adjustable

https://doi.org/10.1017/hpl.2025.32 Published online by Cambridge University Press

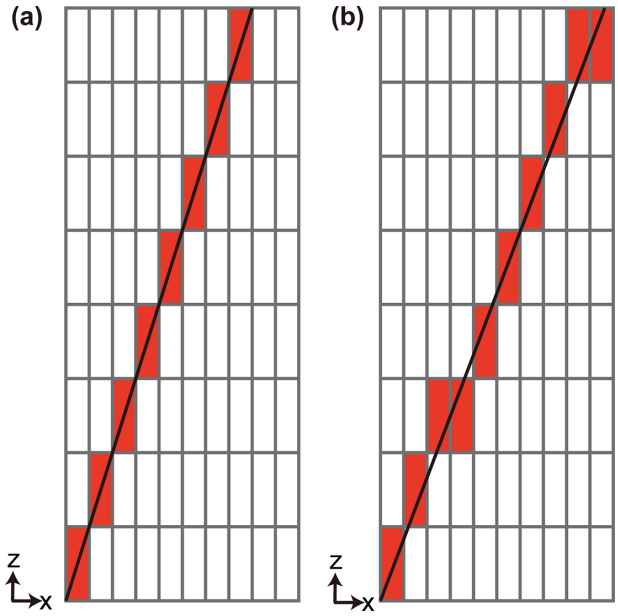


**Figure 2.** Schematic diagram of the propagation of two types of rays in a grid. (a) Grid-matched ray. (b) Non-grid-matched ray.

repetition rate up to 100 Hz, at the beam size of 30 mm × 30 mm, and the intensity distribution of the seed beam has a flat-top profile. Within the gain module, there are two Nd:YAG crystal slabs with doping concentrations of 0.2% and 0.5% (atomic fraction) respectively, each having the dimension of 70 mm × 35 mm × 10 mm, and the long axis is aligned with the [111] orientation. Each Nd:YAG slab is attached by four side surfaces with samarium-doped yttrium aluminum garnet (Sm:YAG) claddings, which have the thickness of 3 mm and an absorption coefficient of 9 $cm^{-1}$ at 1064 nm, that absorb the amplified spontaneous emission (ASE).

The gain module, operating at 1064 nm, is pumped by a 240-bar laser diode array at the central wavelength of 808 nm, with the pulse duration of 300 μs, the spectral bandwidth of 4.5 nm and the maximum pump energy of 36 J. The measured small-signal gain indicates the gain saturation at the pump energy of 28.8 J, due to ASE limitations. The maximum small-signal gain for a single transmission is measured as 3.0 at the incident angle of 40°. The laser system has a compact footprint of 0.6 m × 0.3 m. The two large surfaces of each Nd:YAG slab and the large inner surface of two quartz windows are directly cooled with circulating water, with a total of three cooling layers, each with the thickness of 0.4 mm. Deionized water at 20°C flows in a laminar manner along the *x*-direction at an average speed of 2 m/s for efficient cooling. Thanks to the laminar condition, no significant disturbance effect of the flowing water upon the laser wavefront is observed in the experiment.

As shown in Figure 3, the seed energy of 120 mJ is scaled to 5 J at 10 Hz (operated for 2 minutes with a root-mean-square output energy stability of 1.6%) by the eight-pass

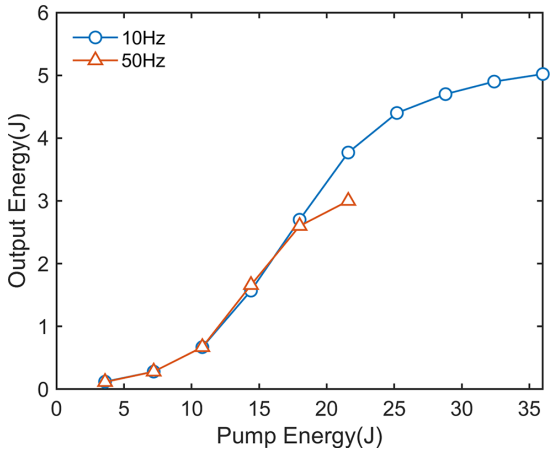


**Figure 3.** Scaling performance of the amplifier at the seed energy of 120 mJ.

amplifier, corresponding to 54% extraction efficiency, as defined as the ratio of extracted energy to stored energy. The stored energy is determined as 9.0 J by the measurement of small-signal gain and model calculations. At the repetition rate of 50 Hz and the pump energy of 21.6 J, the output energy drops to 3 J (operated for 1 minute with a root-mean-square output energy stability of 2.0%) due to thermally induced depolarization at relatively high average power, where the measured depolarization loss is approximately 15%. Output energy at high repetition rate can be further enhanced by using thinner slabs and thus obtaining a reduced temperature rise in the gain medium. The PBS used is a dielectric-coated plate, with an LIDT of 10 J/$cm^2$ at 1064 nm (10 ns pulse width), and all mirrors utilized have dielectric coatings with more than 99.8% reflectivity at 1064 nm and the LIDT of 10 J/$cm^2$. To evaluate system safety, the maximum fluence is monitored throughout the amplification process. The maximum amplified laser fluence reaches 0.43 J/$cm^2$, far below the damage threshold of the gain medium and optics. Post-experiment inspection confirmed no observable damage, ensuring long-term operational stability.

Figure 4 shows the measured amplified output energy of the eight-pass amplifier at 10 Hz versus different seed energy, which agrees well with the simulated results. In comparison to the two-pass and four-pass cases, the eight-pass amplifier has much higher output energy and much faster rises as the input energy increases, reaching the saturation stage at the injection of approximately 100 mJ, while the other two scenarios have no sign of saturation. The comparison demonstrates the distinct advantage of the eight-pass amplifier in both enhancing the amplification efficiency and reducing the input energy requirements. In contrast, the previous approach[15] is only capable of simulating the eight-pass case without angular deviation (i.e., $\alpha = 0$), as illustrated by the dashed line in Figure 4, showing an overestimation of the output energy by 12%.

https://doi.org/10.1017/hpl.2025.32 Published online by Cambridge University Press

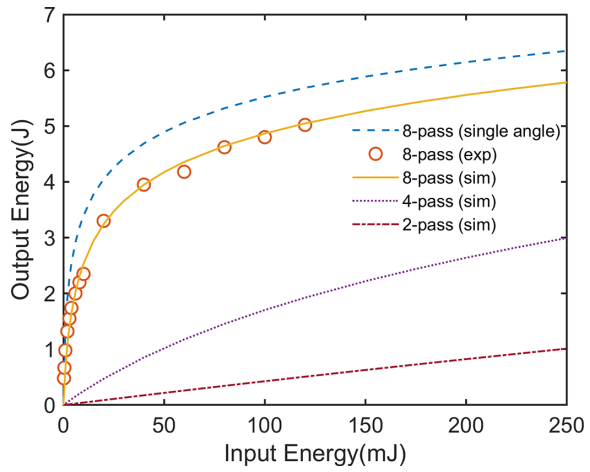


**Figure 4.** Experimental output energy versus input energy for the eight-pass amplifier, compared with the simulation results for two-pass, four-pass and eight-pass configurations, as well as the simulated eight-pass case without angular deviation.

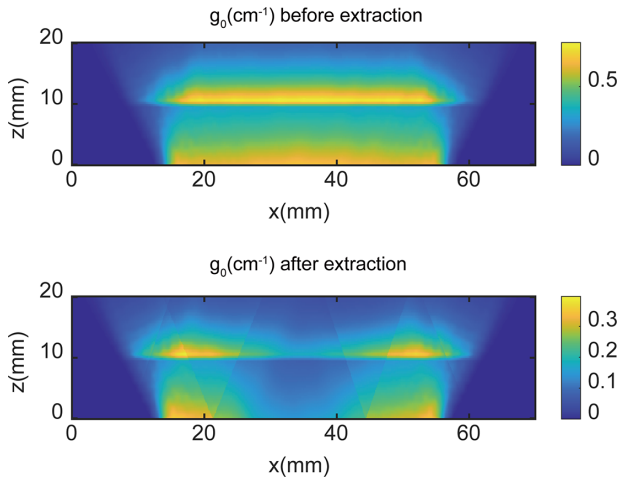


**Figure 5.** The calculation of $g_0$ in the $x$–$z$ plane before and after energy extraction.

The established model of the eight-pass amplifier clearly demonstrates how the spatiotemporal overlap in this amplifier affects the extraction efficiency. Figure 5 compares the two-dimensional distribution of small-signal gain coefficient $g_0$ before and after the beam extraction at the output energy of 4.2 J, while the small-signal gain coefficient averaged through the thickness direction ($z$) is depicted in Figure 6. The experimental results are obtained by directing a probe laser beam through the gain module at the incidence angle of 2.4°. Due to the obstruction caused by mirror M1, only half of the measurement results along the $x$-direction are available. The good agreement between the experimental and simulated results in Figure 6 verifies the validity of the presented model, while the simulated profile (green dotted line) by the previous model without angular deviation suggests a serious deviation from the measured distribution.

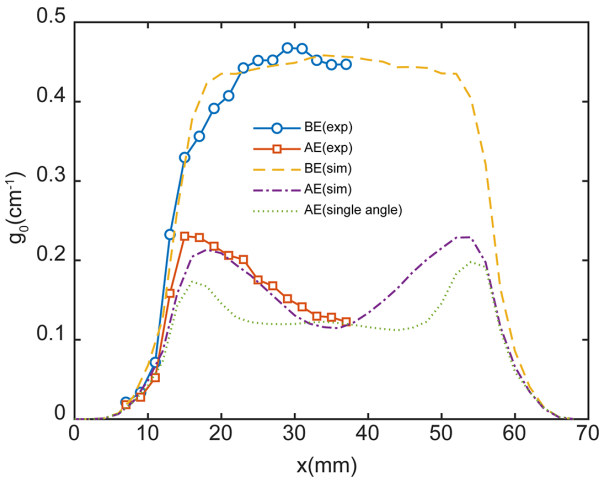


**Figure 6.** The $x$-dimensional profile of $g_0$ averaged over $z$ before and after energy extraction. BE, before extraction; AE, after extraction.

According to Figures 1(b) and 6, the central region ($x$ = 35 mm) where the beam extracts the gain eight times exhibits a marked extraction efficiency of stored energy as high as 71%, close to the simulated value of 75%. In contrast, the regions on the edge ($x$ = 19 mm) with only double passages have the measured extraction efficiency of 44% and the simulated result of 49%.

The diagram of output measurement setup is shown in Figure 7(a), where lens L3 is replaced by a camera for near-field measurement. At the output of 5 J at 10 Hz, the peak-to-valley (PV) value of the wavefront is measured as 1.8λ by using a Shack–Hartmann sensor, while at the output of 3 J and 50 Hz, the PV value is about 5λ, as shown in Figure 7(b). Thanks to the efficient immersion liquid cooling, the wavefront distortion is well controlled, primarily exhibiting a transverse cylindrical component. To correct the wavefront distortion, an adaptive optics system is employed at the output end, leading to the beam quality factor as $\beta_x = 2.16, \beta_y = 2.86$ at 5 J, 10 Hz, and $\beta_x = 2.22, \beta_y = 2.76$ at 3 J, 50 Hz, respectively, with the near-field and far-field pattern illustrated in Figures 7(c) and 7(d).

## 4. Conclusion

In this work, we present a compact Nd:YAG amplifier that utilizes polarization and angular multiplexing to achieve efficient eight-pass transmission. A general spatiotemporal model of the multi-pass amplifier that accounts for the angular multiplexing is established, which plays a crucial role in designing the amplifier parameters and has its validity well verified by the experimental results. The multi-pass amplifier demonstrates an excellent energy scalability that amplifies the seed energy of 120 mJ to 5 J at 10 Hz and 3 J at 50 Hz, having the extraction efficiency of 54% and the beam quality within three times diffraction limit. This

https://doi.org/10.1017/hpl.2025.32 Published online by Cambridge University Press

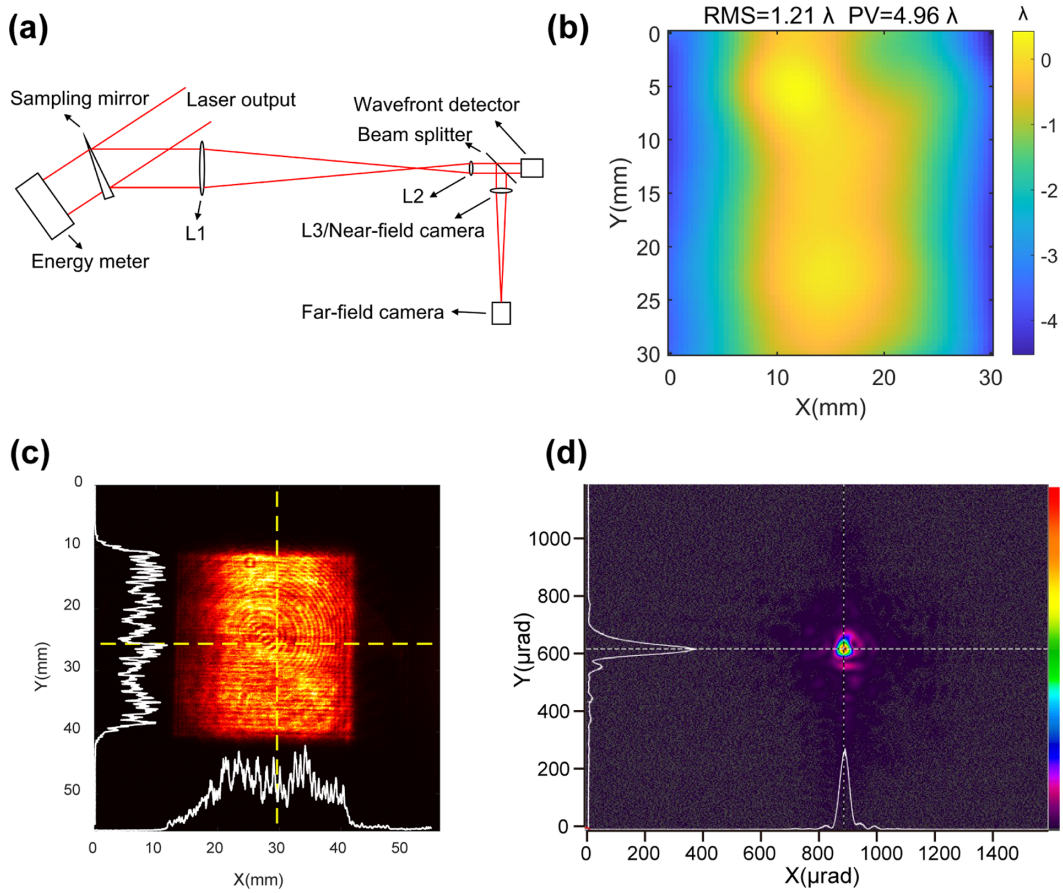


**Figure 7.** Beam quality of amplified output (3 J, 50 Hz). (a) Measurement setup. (b) Beam wavefront. (c) Near-field pattern. (d) Far-field pattern.

work provides a compact and effective multi-pass energy extraction solution while maintaining good beam quality, holding the promise of energy scaling to the tens of joules level.

## Acknowledgements

This work was supported by the National Key Research and Development Program of China (Grant No. 2022YFB3606300) and the Tsinghua University (Department of Precision Instrument)-North Laser Research Institute Co., Ltd. Joint Research Center for Advanced Laser Technology (Grant No. 20216701004).

## References

1. T. Hatae, M. Nakatsuka, H. Yoshida, K. Ebisawa, Y. Kusama, K. Sato, A. Katsunuma, H. Kubomura, and K. Shinobu, Fusion Sci. Technol. **51**, 58 (2007).
2. S. Kalainathan and S. Prabhakaran, Opt. Laser Technol. **81**, 137 (2016).
3. L. Behnke, E. J. Salumbides, G. Göritz, Y. Mostafa, D. Engels, W. Ubachs, and O. Versolato, Opt. Express **31**, 24142 (2023).
4. T. Liu, Z. Sui, L. Chen, Z. Li, Q. Liu, M. Gong, and X. Fu, Opt. Express **25**, 21981 (2017).
5. B. Shi, G. He, J. Mao, F. Wang, K. Yang, B. Zhang, and J. He, Appl. Opt. **60**, 186 (2021).
6. B. M. Van Wonterghem, J. R. Murray, J. H. Campbell, D. R. Speck, C. E. Barker, I. C. Smith, D. F. Browning, and W. C. Behrendt, Appl. Opt. **36**, 4932 (1997).
7. T. Gonçalvès-Novo, D. Albach, B. Vincent, M. Arzakantsyan, and J.-C. Chanteloup, Opt. Express **21**, 855 (2013).
8. T. Hamoudi, H. Chesneau, T. Dubé, E. Dubois, M. Lamy, C. Maunier, A. Braud, C. Meroni, P. Camy, and S. Montant, EPJ Web Conf. **266**, 13015 (2022).
9. Y. Liu, U. Demirbas, M. Kellert, J. Thesinga, H. Cankaya, Y. Hua, L. E. Zapata, M. Pergament, and F. X. Kärtner, OSA Continuum **3**, 2722 (2020).
10. K. Yao, S. Gao, J. Tang, X. Xie, C. Fan, Z. Lu, X. Fu, M. Fan, X. Tian, B. Zhang, X. Sun, D. Xu, K. Zheng, L. Liu, Z. Peng, and J. Su, Appl. Opt. **57**, 8727 (2018).
11. K. Yao, X. Xie, J. Tang, C. Fan, S. Gao, Z. Lu, X. Fu, X. Tian, K. Zheng, M. Fan, and Q. Zhu, Laser Phys. **29**, 115002 (2019).
12. F. Batysta, J. Novák, E. Erdman, E. Sistrunk, A. Vella, T. Galvin, M. Torrance, J. Mambourg, D. Scerbak, C. Byrne, B. Rus, A. Bayramian, K. Schaffers, C. Heinbockel, P. Rosso, D. Gibson, K. Velas, and T. Spinka, Opt. Express **33**, 7372 (2025).
13. K. Schuhmann, M. A. Ahmed, A. Antognini, T. Graf, T. W. Hänsch, K. Kirch, F. Kottmann, R. Pohl, D. Taqqu, A. Voss, and B. Weichelt, Proc. SPIE **9342**, 93420U (2015).
14. C. Wandt, S. Klingebiel, S. Keppler, M. Hornung, M. Loeser, M. Siebold, C. Skrobol, A. Kessel, S. A. Trushin, Z. Major, J. Hein, M. C. Kaluza, F. Krausz, and S. Karsch, Laser Photonics Rev. **8**, 875 (2014).
15. T. Liu, Q. Liu, Z. Sui, M. Gong, and X. Fu, High Power Laser Sci. Eng. **8**, e30 (2020).

https://doi.org/10.1017/hpl.2025.32 Published online by Cambridge University Press